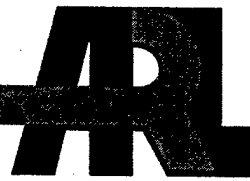


**ARMY RESEARCH LABORATORY**



## **Penetration of a Highly Oblique Steel Plate by a Thin Disk**

**by Nathaniel Bruchey and Kent Kimsey**

**ARL-TR-2828**

**September 2002**

**Approved for public release; distribution is unlimited.**

**20021008 196**

## **NOTICES**

### **Disclaimers**

The findings in this report are not to be construed as an official Department of the Army position unless so designated by other authorized documents.

Citation of manufacturer's or trade names does not constitute an official endorsement or approval of the use thereof.

Destroy this report when it is no longer needed. Do not return it to the originator.

# **Army Research Laboratory**

Aberdeen Proving Ground, MD 21005-5066

---

**ARL-TR-2828**

**September 2002**

## **Penetration of a Highly Oblique Steel Plate by a Thin Disk**

**Nathaniel Bruchey and Kent Kimsey  
Weapons and Materials Research Directorate, ARL**

---

---

## **Abstract**

---

Segmented rod penetrator concepts created interest in the ballistic performance of high-density, low length-to-diameter (L/D) ratio penetrators, but there was a lack of data showing the performance of such thin disks vs. high-obliquity targets. An experimental and computational study was conducted to examine the basic case of a single tungsten heavy alloy disk with an L/D of 1/8 impacting a high-obliquity ( $65^\circ$ ) rolled homogeneous armor steel plate at a nominal velocity of 2 km/s. The study provides valuable insight into the penetration process. Results include depths of penetration and penetration per unit length. Good agreement is seen between the experimental data and the CTH simulation; both show a ricochet phenomenon. Results are also compared to comparable previous studies, and possible explanations for differences are given.

---

## **Contents**

---

<b>List of Figures</b>	<b>v</b>
<b>List of Tables</b>	<b>vii</b>
<b>1. Introduction</b>	<b>1</b>
<b>2. Experiments</b>	<b>1</b>
2.1 Experimental Setup .....	1
2.2 Experimental Results.....	3
<b>3. Numerical Model</b>	<b>9</b>
<b>4. Discussion</b>	<b>12</b>
<b>5. Conclusions</b>	<b>14</b>
<b>6. References</b>	<b>15</b>
<b>Report Documentation Page</b>	<b>17</b>

**INTENTIONALLY LEFT BLANK.**

---

## List of Figures

---

Figure 1. Orientation of plate and shotline. ....	2
Figure 2. Orthogonal striking x-ray radiographs for experiment 1 (shot 1152). ....	4
Figure 3. Orthogonal striking x-ray radiographs for experiment 2 (shot 1153). ....	4
Figure 4. Touchdown x-ray radiographs for experiment 1 (shot 1152) and experiment 2 (shot 1153). ....	5
Figure 5. Fronts of target plates. ....	5
Figure 6. Enlarged view of impact area from first experiment. ....	6
Figure 7. Enlarged view of impact area from second experiment. ....	6
Figure 8. Enlarged view of cross section from first experiment. ....	7
Figure 9. Initial impact conditions (penetrator travels from left to right). ....	10
Figure 10. Impact of disk-shaped penetrator on oblique RHA plate (penetrator travels from left to right). ....	11
Figure 11. Tracer particle axial (X-coordinate direction) velocity time histories. ....	12
Figure 12. Final penetrator and target deformation, $t = 40 \mu\text{s}$ . ....	13

**INTENTIONALLY LEFT BLANK.**

---

## **List of Tables**

---

Table 1. Quasi-static properties of the tungsten alloy.....	2
Table 2. Velocity and attitude values.....	3
Table 3. Crater dimensions. ....	7
Table 4. Johnson-Cook constitutive model parameters. ....	9
Table 5. Crater dimensions comparison of CTH experiment, shot 1.....	13

**INTENTIONALLY LEFT BLANK.**

---

## **1. Introduction**

---

The concept of segmented rod penetrators piqued interest in the penetration performance of high-density, low length-to-diameter (L/D) ratio penetrators impacting steel targets. Several studies have looked at penetration ability as a function of L/D into 0° obliquity, rolled homogeneous armor (RHA) steel. Studies by Herbette (1989), Orphal et al. (1990), and Orphal and Franzen (1990) indicated a trend of increasing penetration per unit length (P/L) with a decreasing L/D at velocities above 1.5 km/s. Bjerke et al. (1992) examined the problem in detail and found a maximum P/L at a L/D of 1/8 for a nominal velocity of 2 km/s. Like previous studies, though, the effort focused on 0° obliquity targets.

Using experimental and computational techniques, the U.S. Army Research Laboratory (ARL) conducted a study to provide valuable insight into the previously unstudied case of a low L/D segment impacting a high-obliquity target plate. The penetration performance of a tungsten heavy alloy (WHA) penetrator with a L/D of 1/8 and a nominal 2-km/s velocity impacting a 65° obliquity RHA steel plate was examined. Experimental and computational results are presented and compared.

---

## **2. Experiments**

---

### **2.1 Experimental Setup**

The projectile consisted of a thin disk of a 91% tungsten alloy affixed with epoxy to a frangible 6/6 nylon pusher sabot. A recess was machined in the front of the sabot to hold the disk. Table 1 gives the properties of the tungsten alloy. The tungsten was swaged to a 25% area reduction. Nominally, the disks had a length of 2.39 mm, a diameter of 19.2 mm, and a mass of 13 g. The resulting L/D of 1/8 was chosen based on the work of Bjerke et al. (1992). The diameter of each sabot was sized appropriately for the 50-mm bore of the gun used. Each had a nominal length of 508 mm and mass of 117 g, giving a total projectile package mass of 130 g.

The target plate was a 464-mm-long × 155-mm-wide, 12.7-mm-thick RHA steel plate. Measured hardness on the Brinell hardness number scale was 321 Bhn. The target differed from targets in previous studies such as Bjerke et al. (1992), which used semi-infinite block targets with a lower hardness in the range of 241–277 Bhn. The plate's normal was positioned 65° relative to the shotline as shown in Figure 1. The shotline was at the horizontal center of the plate and ~80 mm from the top (measured along the face of the plate). The same plate was used for both experiments except that it was turned so that what was the rear bottom in the first experiment became the front top for the second.

Table 1. Quasi-static properties of the tungsten alloy.

Composition (by weight)	Tungsten (91.0%), nickel (6.3%), iron (2.7%)
Density	17,270 kg/m <sup>3</sup>
Hardness (Rockwell hardness C scale)	39.1 R <sub>c</sub>
Tensile properties	
0.2% offset yield strength	1.09 GPa
Ultimate strength	1.11 GPa
Total elongation to failure	9.7%
Compression properties	
0.2% offset yield strength	0.95 GPa
1.0% offset yield strength	1.16 GPa

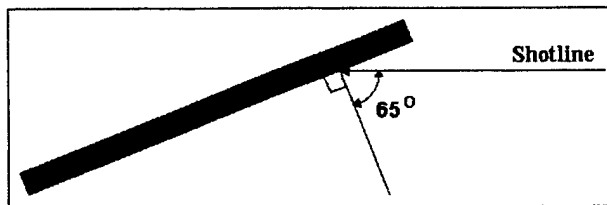


Figure 1. Orientation of plate and shotline.

The experiments were performed at the ARL Experimental Facility 309A. Projectiles were fired from a nominal 50-mm-diameter, 6-m travel, smoothbore powder gun to achieve a nominal velocity of 2 km/s. The target was ~4.8 m from the muzzle. A system of orthogonal 150-kV x-ray radiographs between the muzzle and target allowed determination of the disk velocity, yaw, and pitch. The first set of x-ray heads was ~864 mm uprange from the target, and the second set was 305 mm downrange from the first. A paper break screen positioned ~229 mm uprange of the first x-ray heads served as a trigger to the delay generators for these x-rays. An additional 150-kV x-ray radiograph captured a side view of the projectile striking the target plate. The trigger for this x-ray was a paper break screen backed by 12.7-mm-thick foam placed on the front of the target plate.

A piece of cardboard placed in front of the break screen for the orthogonal x-ray radiographs (~1.09 m in front of the target) served to shatter the frangible nylon sabot. This experimental technique, developed and explained by Bjerke et al. (1992), produces sabot fragments that expand radially and slow down, falling behind the tungsten disk. The tungsten disk typically keeps a low yaw and pitch during its remaining free flight to the target. The technique overcomes the inherent aerodynamic instability of a low L/D right circular cylinder and minimizes the influence of sabot material on the resulting target penetration.

## 2.2 Experimental Results

Two experiments were performed using the setup described in section 2.1. The only variation was a different delay time for the postimpact, or touchdown, x-ray radiographs. The x-ray images were analyzed after each experiment to determine important parameters.

Table 2 shows velocities and attitude values calculated from the x-ray radiographs. A positive pitch represents the top of the disk pitching forward; for yaw, a positive angle represents counterclockwise rotation in the top view. Total yaw is the square root of the sum of the squares of the pitch and yaw. Measurements are from the second flash in the orthogonal x-rays.

Table 2. Velocity and attitude values.

Experiment	Velocity (m/s)	Pitch (°)	Yaw (°)	Total Yaw (°)
1	2135	4	-3	5
2	2140	7	2	7.3

Figures 2–4 show the orthogonal and touchdown x-ray radiographs. The disk is flying right to left. The upper image in Figures 2 and 3 is the top view, and the longer, lower image is the side view. The disk is already in free flight; the nylon sabot is still visible but has been separated and shattered. The touchdown radiographs in Figure 4 have been cropped and enlarged to magnify the region of impact. The delay time (from the break screen on the front of the target) was lengthened 10  $\mu$ s in the second experiment. In the upper image for the first shot, the top of the disk has just begun interacting with the target plate. Some material is already being ejected from the impact crater down along the face of the plate. For the second experiment, approximately one-half to three-quarters of the disk has interacted with the target. The disk has clearly begun to “smear” down the face of the target and eject even more material down the face. The lower portion is still relatively vertical as it was during free flight. There is already a slight indication of a bulge on the rear surface of the target plate.

Figures 5–8 show photographs of the target plate after the shots. Figure 5 shows the full front face. The impact regions are shown enlarged in Figures 6 and 7. Figure 8 shows an enlarged view of the cross-sectioned target from the first experiment.

The disk did not perforate the target in either shot. The frontal views show similar damage patterns in both experiments. Table 3 gives crater measurements. The craters are labeled top to bottom, with the initial hit location being crater 1. The location coordinates are the positions of the approximate centers and are given relative to the lower left plate corner. The actual crater shapes were somewhat ellipsoidal as seen in Figures 5–7. A crater was produced at the initial point of impact and smeared down the face of the plate. At the lower edge of this crater, a relatively straight horizontal lip was formed that was slightly lower than the initial plate surface, but higher than the crater bottom. Below this lip, a second smeared crater was formed. This

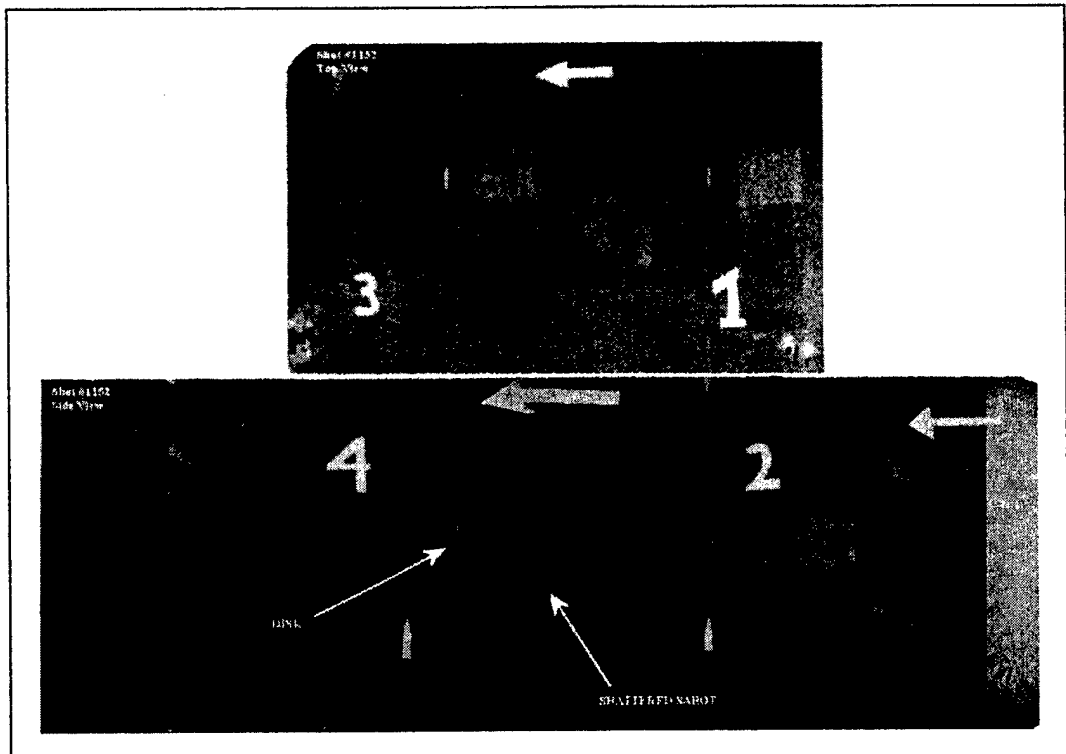


Figure 2. Orthogonal striking x-ray radiographs for experiment 1 (shot 1152).

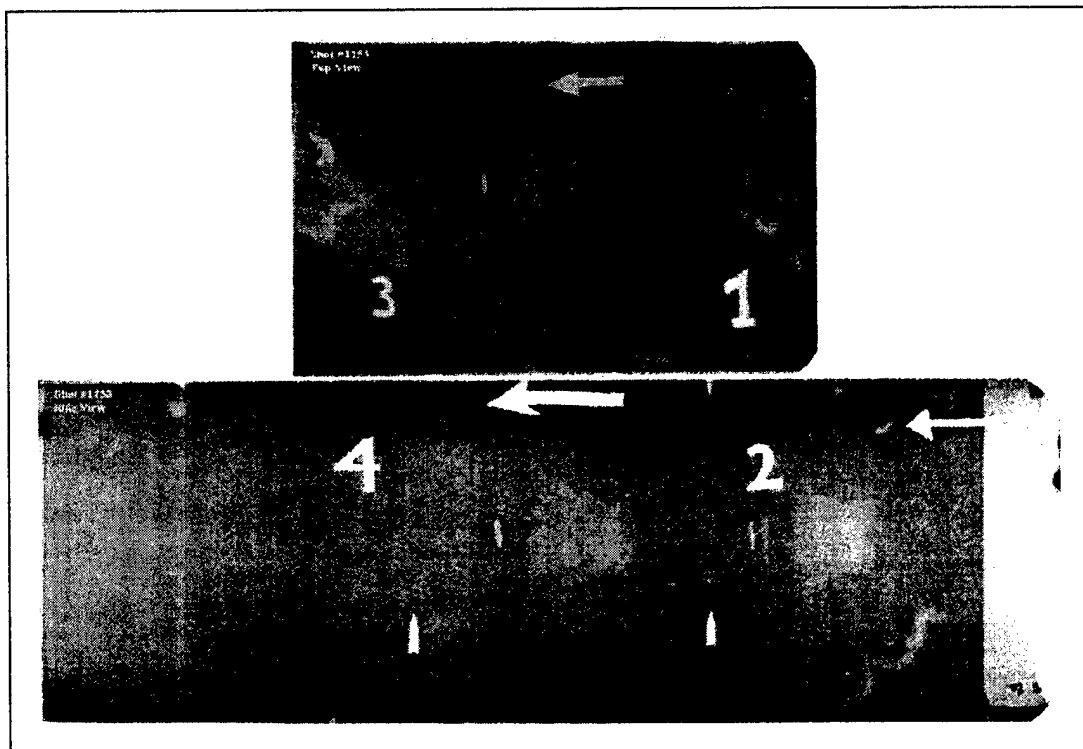


Figure 3. Orthogonal striking x-ray radiographs for experiment 2 (shot 1153).

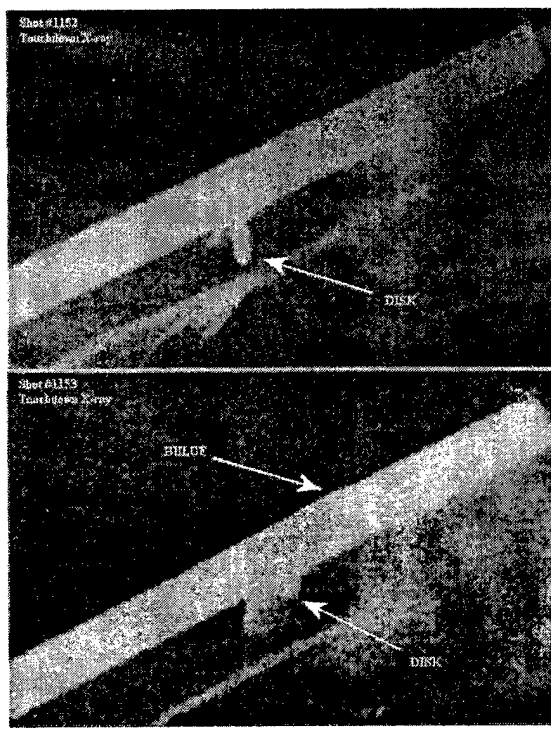


Figure 4. Touchdown x-ray radiographs for experiment 1 (shot 1152) and experiment 2 (shot 1153).

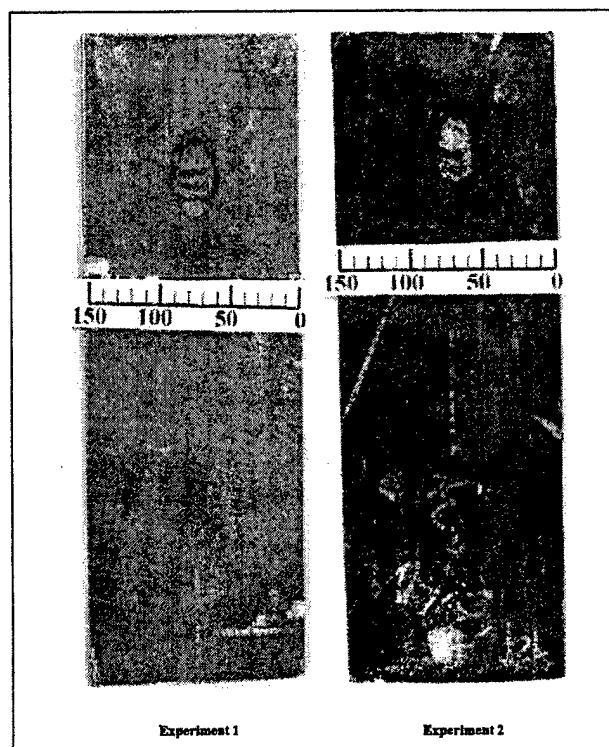


Figure 5. Fronts of target plates.

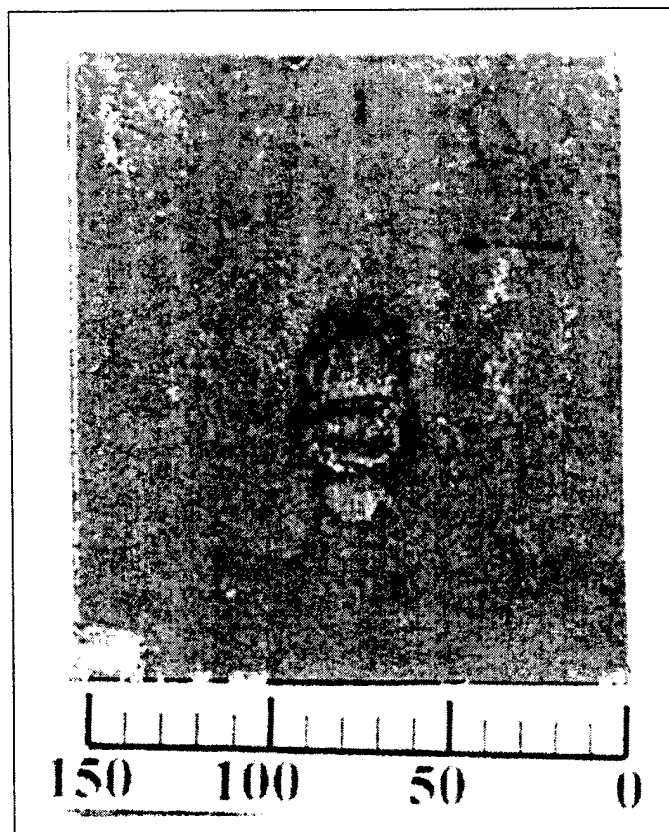


Figure 6. Enlarged view of impact area from first experiment.

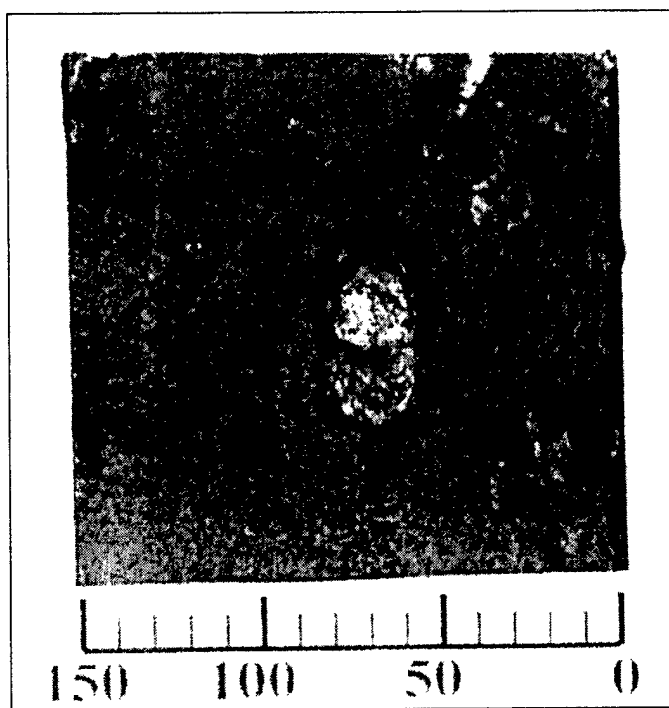


Figure 7. Enlarged view of impact area from second experiment.

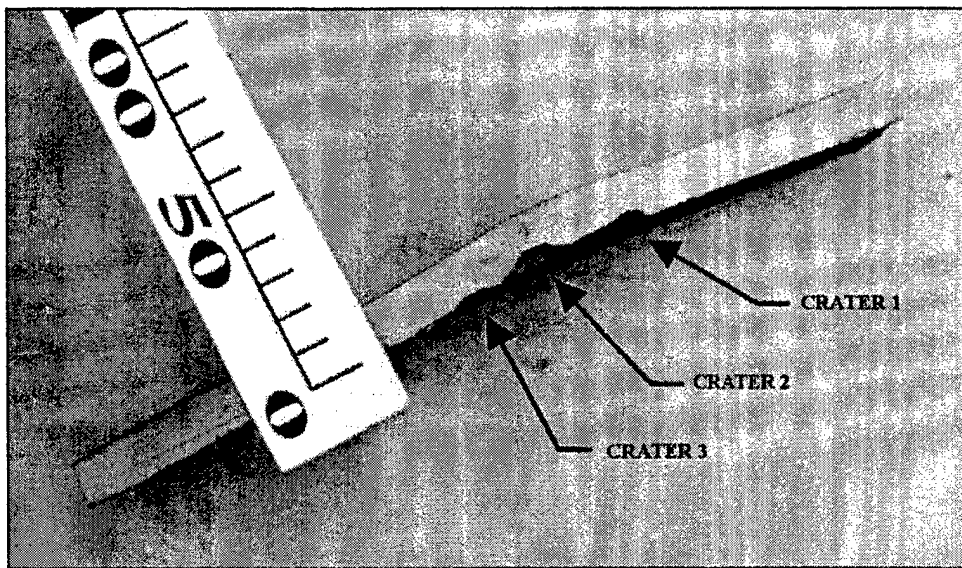


Figure 8. Enlarged view of cross section from first experiment.

Table 3. Crater dimensions.

Experiment	Crater	X Location (mm)	Y Location (mm)	Width (mm)	Length (mm)	DOP (mm)	P/L
1	1	79	382	20	20	2.7	1.1
	2	78	361	24	23	3.7	1.5
	3	77	342	15	11	1.7	0.7
2	1	82	396	22	24	4	1.7
	2	84	371	21	20	3	1.3

Note: DOP = depth of penetration.

pattern of two distinct, yet joined, craters was seen in both experiments. On the first shot, a third crater was formed beneath the second and had significantly smaller dimensions than the first two. The separation of the edges of the second and third craters was greater than that between the first two, but the distances between the centers of each crater were fairly consistent at ~20 mm. The touchdown radiographs supported the smearing action, but did not show the crater formation. From the results though, the multiple craters clearly seem to be characteristic for these impact conditions.

Using these experimental results, an initial explanation of the penetration process was formulated. As the top of the disk first strikes the target, it begins to penetrate the target. Because of the high target obliquity, the disk begins to smear or ricochet down the face of the target. This action, in combination with the circular disk striking the angled target, leads to the ellipsoidal shape of the craters. The impact area of both the disk and target are plastically deformed to failure. The exact nature of the failure is difficult to determine from the results obtained. It is unknown if it is only plastic flow or if some fracturing or other failure occurs. The lower portion of the disk continues to move forward as it had in free flight. As more of the disk interacts with the target, more material is ejected, mainly down the face of the target in the direction of flight. The impact forces exceed the yield strength of the target material and create

plastic waves that move through the target to produce the large bulging and warping of the plate. The gross plastic deformation does not show up until later in the process. This delay is evidenced by the lack of bulging in the touchdown x-ray radiograph for the first experiment and the bulge showing at the later time of the second radiograph. The underlying reasons for formation of multiple craters is not clearly evident from the experimental results. It may be explained as the disk ricocheting along the surface, like a rock skipping across the surface of water. Another possibility is that a presence of target material in front of the disk causes the disk to fail along a line parallel to the line of flight. As the remaining lower portion of the disk slips over the ridge in the target, it begins creating the next crater. New craters continue to form until the entire disk has impacted.

DOPs and P/L values are also shown in Table 3. The target plate in the crater area for the first shot was sectioned to yield accurate DOPs. Measurements of the amount of material remaining were taken normal to the rear plate surface at the deepest point of penetration. The DOP is the original plate thickness minus the measured amount of material remaining. The crater area for the second shot was left intact for future examination; therefore, the DOPs are more approximate. A gauge was inserted into the crater to measure the depth relative to the estimated location of the original front target surface at the crater. In addition to the craters, the impacting disks formed large-area bulges with ~8-mm peaks on the rear of both plates. The initial stages of this bulging were seen on the touchdown radiograph for the second shot.

For similar penetrators impacting normal incidence, semi-infinite RHA, the values of P/L reported in Bjerke et al. (1992) were higher, where values ranged from 4 to 6 for a L/D of 1/8. A possible explanation for the lower values seen with the high-obliquity targets lies in the physics involved with thin-disk impacts and penetrators. The penetration benefits seen with thin disks result from the high-shock pressure created at the interface during planar impacts. Because of the low L/D, the high pressure remains throughout much, if not all, of the penetration process. When the impact is no longer planar, as with these high-obliquity targets, a shock wave is no longer produced in the disk. Without the high pressures, the disk cannot penetrate as effectively. Although this is felt to be the main explanation for the lower P/L values, the thinness of this target and the higher hardness could contribute to a lesser degree.

After two experiments producing similar results, a complementary numerical simulation was performed. The computational study would allow more detailed study of the process, possibly answering some of the questions still remaining from the experiments.

---

### 3. Numerical Model

---

The numerical study was conducted with the Eulerian wave propagation code CTH (McGlaun and Thompson 1990). A single program multiple data (SPMD) paradigm with explicit message passing between computational subdomains was used to map the global computational domain onto a scalable architecture (Kimsey et al. 1998). CTH is a family of computer programs for modeling solid dynamics problems involving shock wave propagation, multiple materials, and large deformations in one, two, and three dimensions. CTH employs a two-step solution scheme—a Lagrangian step followed by a remap step. The conservation equations are replaced by explicit finite volume equations that are solved in the Lagrangian step. The remap step uses operating splitting techniques to replace multidimensional equations with a set of one-dimensional equations. The remap or advection step is based on a second order accurate van Leer scheme. To minimize material dispersion, a high-resolution material interface tracker is available. Both analytical and tabular equations-of-state are available to model the hydrodynamic behavior of materials. Models for elastic-plastic behavior and high-explosive detonation are available also.

The CTH simulations reported herein used a linear Hugoniot shock-particle velocity equation-of-state to model the hydrodynamic behavior of the materials. The Johnson-Cook constitutive model (Johnson and Cook 1983), which includes the effects of strain hardening, strain rate hardening, and thermal softening, was used to define the von Mises flow stress. Table 4 lists Johnson-Cook parameters used for the WHA and the RHA. The Johnson-Cook damage model (Johnson and Cook 1983) was used to model material fracture. The simulations used a three-dimensional Cartesian coordinate system. The multiple material temperatures and pressures thermodynamic model was used to calculate temperatures and pressures for each material in multimaterial cells. The Sandia Modified Young's Reconstruction Algorithm (SMYRA) (Bell and Hertel 1992) was used to track material interfaces and minimize material dispersion in multimaterial cells.

Table 4. Johnson-Cook constitutive model parameters.

Material	A (GPa)	B (GPa)	n	C	m
WSM	1.51	0.18	0.12	0.016	1.0
RHA	0.98	1.69	0.754	0.00435	0.8

The Johnson-Cook initial yield strength, parameter A, was modified for plate thickness in the Johnson-Cook model for RHA to reproduce the variation of static yield strength as indicated by hardness changes (Benck 1976; Benck and Robitaille 1977). The value of the A parameter for RHA was computed using the procedure documented by Meyer and Kleponis (2001). The A parameter value listed in Table 4 for RHA is the approximate static yield for 12.7-mm RHA.

The geometries of the WHA disk-shaped penetrator and the RHA target plate modeled in CTH were identical to the geometries used in the experiments. The penetrator was assigned an initial impact speed of 2.135 km/s (shot 1152 impact speed) in the positive X-coordinate direction. Figure 9 shows the initial impact conditions modeled in the numerical study. The computational mesh is composed of 0.3-mm cubic cells in the region of the disk-target interaction region with a geometric cell expansion to extend the mesh to the boundaries of the computational domain. The 0.3-mm cubic cell subgrid region spanned from -4.1 to 4.86 cm in the X-coordinate direction, from -1.96 to 1.44 cm in the Y-coordinate direction, and from 0.0 to 0.9 cm in the Z-coordinate direction. The constant subgrid region results in eight cells through the thickness of the disk-shaped penetrator. The global computational domain was composed of 4.8 million cells that were mapped onto 32 IBM SP Power3 processors. The X-Y plane is modeled as a symmetry boundary to minimize the size of the computational mesh. Shown also in Figure 9 are nine Lagrangian tracer particles defined along the disk midplane and parallel to the Y-coordinate axis. The tracer particles are used to collect flow field data as a function of time. The tracer particle data are used to gain insight into material response during the impact event.

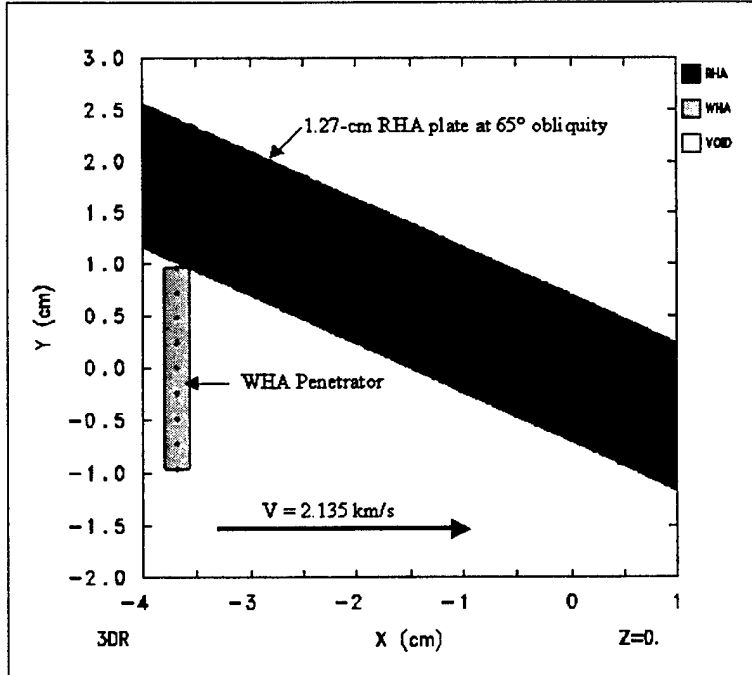


Figure 9. Initial impact conditions (penetrator travels from left to right).

A series of plots depicting material location during the impact event is shown in Figure 10. The plots correspond to the initial configuration and 5, 10, and 20  $\mu$ s after contact with the target plate. The initial impact crater is formed by the interaction of the top edge of the disk-shaped penetrator with the oblique target plate (see Figure 10b). After the formation of the initial impact crater, the penetration channel is lengthened as additional penetrator material impacts the target. At 10  $\mu$ s, the material plot (Figure 10c) shows penetrator material coating the impact face of the target and the initial formation of a second impact crater lip. As additional penetrator material

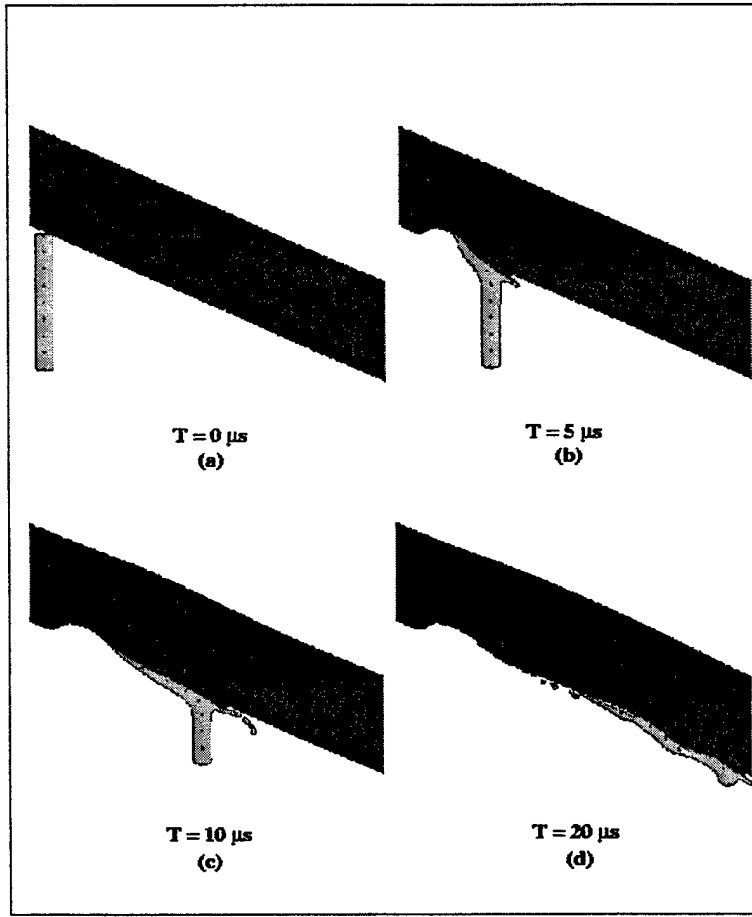


Figure 10. Impact of disk-shaped penetrator on oblique RHA plate  
(penetrator travels from left to right).

impacts the target, penetrator material continues to coat the impact face of the target and penetrator material begins to flow over the second crater lip (Figure 10c). As additional penetrator material flows over the second crater lip, the formation of a third impact crater can be seen in the material plot at 20  $\mu$ s (Figure 10d).

The material plots shown in Figure 10 suggest a ricochet penetration phenomenon.

The time histories of the axial (X-coordinate direction) velocity component for each tracer particle are plotted in Figure 11. The time history data for each tracer particle were recorded at an interval of 0.1  $\mu$ s. The velocity-time histories shown in Figure 11 span the initial 20  $\mu$ s of the impact event. The time histories show that the tracers located near the top edge of the disk-shaped penetrator are the first to decrease in axial velocity. The tracer particle located at the bottom edge of the disk-shaped penetrator does not show a decrease in axial velocity until  $\sim$ 18  $\mu$ s after the top edge of the disk impacts the target.

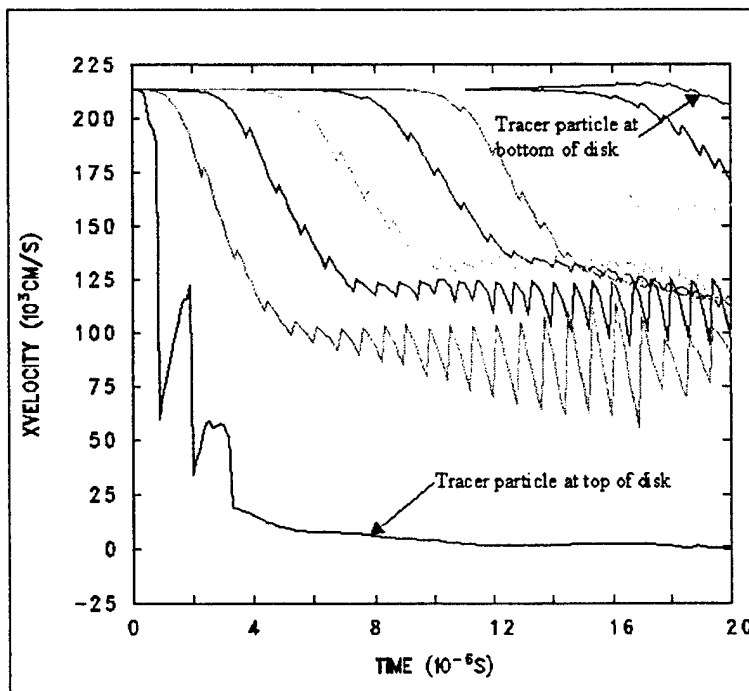


Figure 11. Tracer particle axial (X-coordinate direction) velocity time histories.

Figure 11 also shows that the tracer particle located at the top edge of the disk-shaped penetrator comes to rest in the initial impact crater at  $\sim 12 \mu\text{s}$  after impact. All other tracer particle axial velocities shown in Figure 11 do not exhibit a rapid decay to zero due to momentum transfer to the target plate. The momentum transfer produces a slight bulge on the rear surface of the target plate as evident in Figure 12.

#### 4. Discussion

Table 5 provides a comparison between experimental data and the CTH simulation for characteristic crater dimensions. The material plot shown in Figure 10d shows the formation of three distinct impact craters. The second and third impact craters at  $40 \mu\text{s}$  (Figure 12) are less distinguishable. The predicted DOPs for the second and third impact craters are much shallower than the measured DOPs. The predicted DOP for the first crater is within 5.6% of the measured DOP. The predicted crater length for each impact crater shows good agreement with measured values. The simulations suggest a total projectile-target interaction length of 54 mm, which compares well with the measured value of 54 mm. While the simulation does not capture the details of the second and third impact craters, it does predict a ricochet impact event as was observed in the experiments.

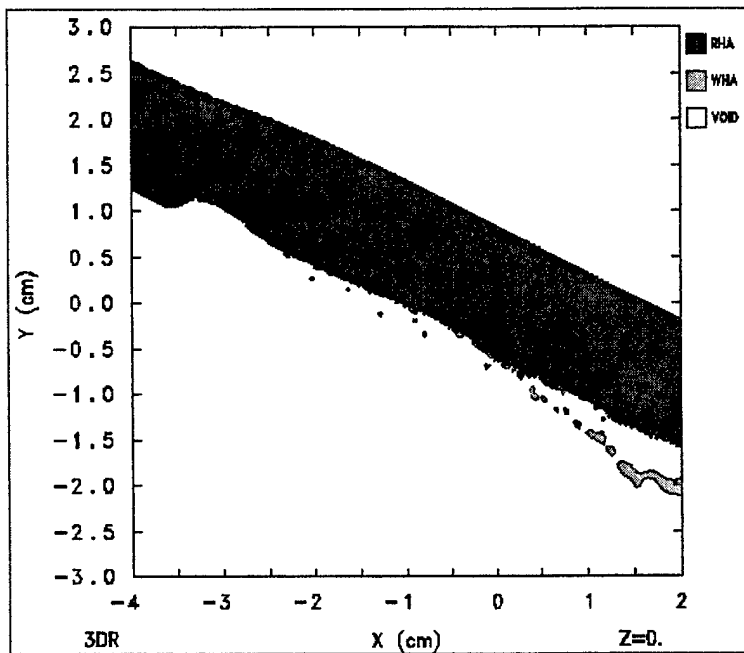


Figure 12. Final penetrator and target deformation,  $t = 40 \mu\text{s}$ .

Table 5. Crater dimensions comparison of CTH experiment, shot 1.

Crater	Length (mm)	DOP (mm)
1	15.0	2.85
	20.0	2.70
2	26.7	1.43
	23.0	3.70
3	12.3	0.83
	11.0	1.70

The penetration phenomena observed in both the simulations and the experiments suggest that a steady-state penetration phase (commonly observed in normal incidence impact scenarios) does not occur in disk-shaped penetrators impacting high-obliquity targets. In addition, the tracer particle data shown in Figure 11 show that until a tracer particle impacts the target its axial velocity component remains constant. Additional simulations and experiments need to be conducted to characterize the influence of penetrator L/D ratio and target obliquity on the duration of the steady penetration phase. In addition, both the simulations and the experiments suggest that disk-shaped penetrators with an L/D ratio of 1/8 are not very efficient against high-obliquity targets.

---

## **5. Conclusions**

---

A combined computational and experimental study has been conducted to examine the impact dynamics of a high-velocity (2.1 km/s) disk-shaped penetrator impacting a high-obliquity ( $65^\circ$ ) steel target. The L/D ratio of the disk-shaped penetrator is 1/8. Both the experiments and the simulation show a ricochet penetration event with multiple impact craters on the impact face of the target. The simulation suggests that the multiple impact craters are formed due to penetrator material flowing over the first and second impact crater lips. Comparison of characteristic crater dimensions between experimental measurements and the simulation are in good agreement.

Based on the results of this study, areas of future investigation might address a range of plate obliquities to determine the critical obliquity angle for transition from penetration to a ricochet impact event and multiple disk impacts on a high-obliquity target.

---

## 6. References

---

- Bell, R. L., and E. S. Hertel, Jr. "An Improved Material Interface Reconstruction Algorithm for Eulerian Codes." SAND92-1716, Sandia National Laboratories, Albuquerque, NM, September 1992.
- Benck, R. F. "Quasi-Static Tensile Stress-Strain Curves – II. Rolled Homogeneous Armor." BRL-MR-2703, U.S. Army Ballistic Research Laboratory, Aberdeen Proving Ground, MD, 1976.
- Benck, R. F., and J. L. Robitaille. "Tensile Stress-Strain Curves – III. Rolled Homogeneous Armor at a Strain Rate of 0.42 s-1." BRL-MR-2760, U.S. Army Ballistic Research Laboratory, Aberdeen Proving Ground, MD, 1977.
- Bjerke, T. W., J. A. Zukas, and K. D. Kimsey. "Penetration Performance of Disk Shaped Penetrators." *International Journal of Impact Engineering*, vol. 12, pp. 263–280, 1992.
- Herbette, G. "The Influence of Projectile Shape on Penetration Power." Eleventh International Symposium on Ballistics, Brussels, Belgium, 1989.
- Johnson, G. R., and W. H. Cook. "A Constitutive Model and Data for Metals Subjected to Large Strains, High Strain Rates, and High Temperatures." *Proceedings of the 7th International Symposium on Ballistics*, The Hague, The Netherlands, pp. 541–547, 1983.
- Kimsey, K. D., S. J. Schraml, and E. S. Hertel. "Scalable Computations in Penetration Mechanics." *Advances in Engineering Software*, vol. 29, pp. 209–216, 1998.
- McGlaun, J. M., and S. L. Thompson. "CTH: A Three-Dimensional Shock Wave Physics Code." *International Journal of Impact Engineering*, vol. 10, pp. 351–360, 1990.
- Meyer, H., and D. Kleponis. "An Analysis of Parameters for the Johnson-Cook Strength Model for 2-in-Thick Rolled Homogeneous Armor." ARL-TR-2528, U.S. Army Research Laboratory, Aberdeen Proving Ground, MD, June 2001.
- Orphal, D. L., C. E. Anderson, and R. R. Franzen. "Impact Calculations of L/D ≤ 1 Penetrators." Twelfth International Symposium on Ballistics, San Antonio, TX, 1990.
- Orphal, D. L., and R. R. Franzen. "Penetration Mechanics and Performance of Segmented Rods Against Metal Targets." *International Journal of Impact Engineering*, vol. 10, pp. 427–438, 1990.

**INTENTIONALLY LEFT BLANK.**

REPORT DOCUMENTATION PAGE			Form Approved OMB No. 0704-0188
<p>Public reporting burden for this collection of information is estimated to average 1 hour per response, including the time for reviewing instructions, searching existing data sources, gathering and maintaining the data needed, and completing and reviewing the collection of information. Send comments regarding this burden estimate or any other aspect of this collection of information, including suggestions for reducing this burden, to Washington Headquarters Services, Directorate for Information Operations and Reports, 1215 Jefferson Davis Highway, Suite 1204, Arlington, VA 22202-4302, and to the Office of Management and Budget, Paperwork Reduction Project(0704-0188), Washington, DC 20503.</p>			
1. AGENCY USE ONLY (Leave blank)	2. REPORT DATE	3. REPORT TYPE AND DATES COVERED	
	September 2002	Final, September 2001–June 2002	
4. TITLE AND SUBTITLE		5. FUNDING NUMBERS	
Penetration of a Highly Oblique Steel Plate by a Thin Disk		1L162618AH80	
6. AUTHOR(S)			
Nathaniel Bruchey and Kent Kimsey			
7. PERFORMING ORGANIZATION NAME(S) AND ADDRESS(ES)		8. PERFORMING ORGANIZATION REPORT NUMBER	
U.S. Army Research Laboratory ATTN: AMSRL-WM-TC Aberdeen Proving Ground, MD 21005-5066		ARL-TR-2828	
9. SPONSORING/MONITORING AGENCY NAMES(S) AND ADDRESS(ES)		10. SPONSORING/MONITORING AGENCY REPORT NUMBER	
11. SUPPLEMENTARY NOTES			
12a. DISTRIBUTION/AVAILABILITY STATEMENT		12b. DISTRIBUTION CODE	
Approved for public release; distribution is unlimited.			
13. ABSTRACT (Maximum 200 words)			
Segmented rod penetrator concepts created interest in the ballistic performance of high-density, low length-to-diameter (L/D) ratio penetrators, but there was a lack of data showing the performance of such thin disks vs. high-obliquity targets. An experimental and computational study was conducted to examine the basic case of a single tungsten heavy alloy disk with an L/D of 1/8 impacting a high-obliquity (65°) rolled homogeneous armor steel plate at a nominal velocity of 2 km/s. The study provides valuable insight into the penetration process. Results include depths of penetration and penetration per unit length. Good agreement is seen between the experimental data and the CTH simulation; both show a ricochet phenomenon. Results are also compared to comparable previous studies, and possible explanations for differences are given.			
14. SUBJECT TERMS		15. NUMBER OF PAGES	
thin disk, low L/D, high-obliquity, tungsten, WHA, RHA, segmented rod penetrator, CTH simulation		21	
		16. PRICE CODE	
17. SECURITY CLASSIFICATION OF REPORT	18. SECURITY CLASSIFICATION OF THIS PAGE	19. SECURITY CLASSIFICATION OF ABSTRACT	20. LIMITATION OF ABSTRACT
UNCLASSIFIED	UNCLASSIFIED	UNCLASSIFIED	UL

**INTENTIONALLY LEFT BLANK.**